Implications of postseismic gravity change following the great 2004 Sumatra-Andaman earthquake from the regional harmonic analysis of GRACE intersatellite tracking data

Shin-Chan Han,[1,2] Jeanne Sauber,[1] Scott B. Luthcke,[1] Chen Ji,[3] and Fred F. Pollitz[4]

Received 19 March 2008; revised 23 July 2008; accepted 21 August 2008; published 26 November 2008.

[1] We report Gravity Recovery and Climate Experiment (GRACE) satellite observations of coseismic displacements and postseismic transients from the great Sumatra-Andaman Islands (thrust event; $M_w \sim 9.2$) earthquake in December 2004. Instead of using global spherical harmonic solutions of monthly gravity fields, we estimated the gravity changes directly using intersatellite range-rate data with regionally concentrated spherical Slepian basis functions every 15-day interval. We found significant step-like (coseismic) and exponential-like (postseismic) behavior in the time series of estimated coefficients (from May 2003 to April 2007) for the spherical Slepian functions. After deriving coseismic slip estimates from seismic and geodetic data that spanned different time intervals, we estimated and evaluated postseismic relaxation mechanisms with alternate asthenosphere viscosity models. The large spatial coverage and uniform accuracy of our GRACE solution enabled us to clearly delineate a postseismic transient signal in the first 2 years of postearthquake GRACE data. Our preferred interpretation of the long-wavelength components of the postseismic gravity change is biviscous viscoelastic flow. We estimated a transient viscosity of 5×10^{17} Pa s and a steady state viscosity of 5×10^{18}–10^{19} Pa s. Additional years of the GRACE observations should provide improved steady state viscosity estimates. In contrast to our interpretation of coseismic gravity change, the prominent postearthquake positive gravity change around the Nicobar Islands is accounted for by seafloor uplift with less postseismic perturbation in intrinsic density in the region surrounding the earthquake.

Citation: Han, S.-C., J. Sauber, S. B. Luthcke, C. Ji, and F. F. Pollitz (2008), Implications of postseismic gravity change following the great 2004 Sumatra-Andaman earthquake from the regional harmonic analysis of GRACE intersatellite tracking data, *J. Geophys. Res.*, *113*, B11413, doi:10.1029/2008JB005705.

1. Introduction

[2] The great 26 December 2004 Sumatra-Andaman earthquake ruptured an approximately 1500 km long and 150 km wide portion of the boundary between the Indo-Australian and Burma plates [*Chlieh et al.*, 2007; *Ammon et al.*, 2005, and references therein]. Constraining the complex response of the Earth to this great earthquake is important for understanding the rheology of the crust and mantle and for estimating subsequent earthquake hazard in the surrounding region. The large spatial extent and magnitude of this event makes it well suited for study with gravity measurements from the Gravity Recovery and Climate Experiment (GRACE) satellites [*Tapley et al.*, 2004a]. Additionally, GRACE data are sensitive to both the surface uplift or subsidence and interior strain (density) variation and cover a broad area including both land and ocean with uniform accuracy and continuous sampling [*Han et al.*, 2006]. In our earlier studies [*Han et al.*, 2006; *Han and Simons*, 2008] we hypothesized that the coseismic GRACE results were best accounted for by dilatation of the crust along with gravity change due to coseismic uplift. *Panet et al.* [2007] and *Chen et al.* [2007] reported positive postseismic gravity change by analyzing monthly global harmonic fields. *Ogawa and Heki* [2007] suggest that the postseismic geoid change might be due to upper mantle water diffusion following the earthquake. The latter three studies were based on spatial filtering of monthly gravity solutions that yielded the gravity signatures with coarse resolutions in space and time. The results of this approach lead to smaller amplitudes of the earthquake deformation than the results from the direct analysis of satellite tracking data (*Han et al.* [2006] and this study) or the spatiospectral localization [*Han and Simons*, 2008]. All of these results complement studies that have used seismological and discrete surface measurements obtained from GPS, tide gauges and InSAR [*Hsu et al.*, 2006; *Pollitz et al.*, 2006; *Chlieh et*

[1]Planetary Geodynamics Laboratory, NASA Goddard Space Flight Center, Greenbelt, Maryland, USA.
[2]Goddard Earth Science and Technology Center, University of Maryland, Baltimore County, Baltimore, Maryland, USA.
[3]Department of Earth Sciences, University of California, Santa Barbara, California, USA.
[4]U.S. Geological Survey, Menlo Park, California, USA.

Copyright 2008 by the American Geophysical Union.
0148-0227/08/2008JB005705$09.00

al., 2007]. To maximize the scientific return of GRACE data for this regional study of the response to this massive earthquake, we developed a localized analysis approach using alternative basis functions.

[3] Spherical harmonic functions are the solutions of the Laplace equation defined on and above a sphere containing the source region. They are orthogonal basis functions and have been used to model Earth's and other planets' gravitational and magnetic potential fields from satellite tracking data and from onboard measurements. For analyzing data from the GRACE satellite mission, the spherical harmonic basis functions have been used to generate monthly mean geopotential fields [*Tapley et al.*, 2004a]. From years of GRACE data, the spherical harmonic representation has successfully modeled the mean geopotential field with a 100-fold improvement over limited spectral bands [*Tapley et al.*, 2004a]. In addition to the accurate mean gravity field, the monthly averaged gravity fields have been also computed for more than 5 years since mid-2002 and the temporal variations in such monthly fields have been interpreted as the result of mass redistribution on the Earth's surface. Various effects may contribute to temporal mass variations detected by GRACE satellite data; these processes include terrestrial and ocean water mass fluctuations, ice mass variation, postglacial rebound, and earthquake-triggered change. The only way to discriminate the appropriate geophysical sources or reasons responsible for the gravity (mass) variation is to analyze the anomaly in association with its geographical location and temporal pattern. For example, the seasonally changing gravity in the Amazon area is interpreted as terrestrial water storage fluctuations [*Tapley et al.*, 2004b]. The gradual increase (positive linear trend) in gravity variation near the Hudson Bay has been attributed to ongoing postglacial rebound following the removal of the Canadian Laurentide ice sheet [*Tamisiea et al.*, 2007]. The decreasing anomalies (negative linear trend) in the southeast coastal regions of Greenland and west Antarctica, and southern Alaska are understood to be due to recent ice mass loss [*Luthcke et al.*, 2006a].

[4] The spatiospectral localization may be suitable to delineate the specific anomalies associated with certain geographical regions from the global spherical harmonic coefficients [*Simons et al.*, 1997]. This technique essentially involves spectral smoothing, in contrast with methods based on spatial smoothing. For example, *Han and Simons* [2008] identified the abrupt gravity change that was caused by the 2004 Sumatra-Andaman earthquake from each of the monthly GRACE geopotential coefficients after suppressing the contributions from other regions.

[5] In this study, we enhance the approach to estimate the earthquake-triggered signals by using the satellite tracking data directly over the region where the signal of interest is supposed to be dominant and by incorporating the new basis functions that are regionally concentrated and satisfy the harmonic condition (or upward and downward continuation). The resulting coefficients of each regional basis function are naturally expected to include the gravity changes caused by the earthquake and other geophysical signals associated only with the region as well. Unlike the global coefficients, the regional coefficients would not be influenced by undesired signals such as Amazon hydrology but would be affected by the climate signals originating around the earthquake region. However, the earthquake signal can be differentiated from the climate signals due to the distinct seasonal characteristics of climate signals. Therefore, the earthquake signal is separated geographically by regional basis function and temporally by time series analysis.

[6] In the following sections, we first introduce the characteristics of new basis functions and show the analysis results at 15-day intervals for the time period from May 2003 to April 2007 and then we analyzed earthquake related signals observed in the GRACE gravity results. Specifically, the observed long-wavelength postseismic gravity change result was compared to the predicted signal based on alternate viscosity structures and physical models.

2. Band-Limited Spherical Basis Functions Concentrated on the Sumatra Region

[7] We employed a method given by *Simons and Dahlen* [2006] to obtain a set of spherical Slepian basis functions [after *Slepian*, 1983] that are an alternative to the standard spherical harmonic solutions. The Slepian basis functions are band-limited orthogonal harmonic functions and their energy is optimally concentrated on a predefined area on the Earth's surface. They are constructed by linear combination of (usual) spherical harmonic functions, thus preserving the harmonic condition on the globe. Following *Simons and Dahlen* [2006], we express a (band-limited) signal $s(\theta, \lambda)$ in terms of usual spherical harmonic basis and Slepian basis as follows:

$$s(\theta,\lambda) = \sum_{l=0}^{L} \sum_{m=-l}^{l} s_{lm} Y_{lm}(\theta,\lambda) = \sum_{n=1}^{(L+1)^2} s_n g_n(\theta,\lambda), \qquad (1)$$

where $Y_{lm}(\theta, \lambda)$ is the spherical harmonic function of degree l and order m and $g_n(\theta, \lambda)$ is the nth Slepian function, expressed as $g_n(\theta, \lambda) = \sum_{l=0}^{L} \sum_{m=-l}^{l} g_{n,lm} Y_{lm}(\theta, \lambda)$. That is, the nth Slepian function is determined on the basis of spherical harmonic functions with the expansion coefficient of $g_{n,lm}$. The new basis functions are determined by maximizing the power ratio, γ, between its energy within a given area (for example, $\theta_1 \le \theta \le \theta_2$ and $\lambda_1 \le \lambda \le \lambda_2$) and the energy within the entire globe as follows:

$$\gamma = \int_{\lambda_1}^{\lambda_2} \int_{\theta_1}^{\theta_2} g^2(\theta,\lambda) \sin\theta d\theta d\lambda \Big/ \int_{0}^{2\pi} \int_{0}^{\pi} g^2(\theta,\lambda) \sin\theta d\theta d\lambda. \qquad (2)$$

γ is the ratio indicating the quality of spatial concentration of the function $g(\theta, \lambda)$. The maximization of the concentration ratio γ can be solved equivalently in spectral domain given by

$$\mathbf{Dg} = \gamma \mathbf{g}, \qquad (3)$$

where the elements of the matrix **D** are the integrals of the product of two spherical harmonic functions over the given

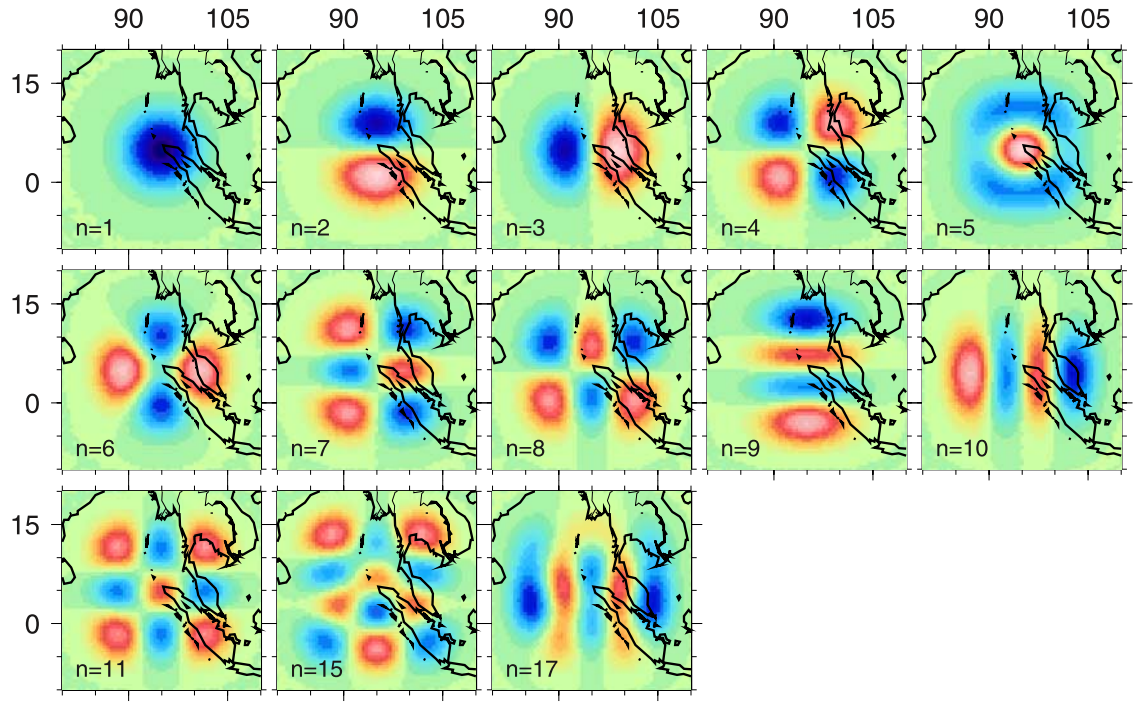

Figure 1. Spatial maps for some of the well-concentrated basis functions between 10°S and 20°N and 80°E and 110°E. The blue and red colors indicate negative and positive gravity changes, respectively. The global integral of the squares of each function is normalized to be 1. The integration of multiplication of two different functions is equal to zero, indicating mutual orthogonality.

area as also explicitly shown in equation (33) of *Simons and Dahlen* [2006]. The resulting eigenvalue of equation (3) is the concentration ratio and the eigenvector **g** includes the spherical harmonic coefficients of the desired Slepian basis function $g(\theta, \lambda)$. If the area of interest can be defined with a polar radius (colatitude) after a certain coordinate rotation, like a polar cap region, the matrix **D** is a sparse block-diagonal matrix and thus the eigen problem can be easily solved. Furthermore, the eigenvector can be solved using a simple tridiagonal matrix that commutes with the matrix **D** [see also *Simons and Dahlen*, 2006]. If the region of interest is irregular such as the "rectangular" region used in equation (2), all the elements in the matrix **D** need to be computed explicitly.

[8] The spherical harmonic coefficients s_{lm} and Slepian coefficients s_n are related through the eigenvectors of **D** as follows:

$$s_{lm} = \sum_{n=1}^{(L+1)^2} s_n g_{n,lm}, \tag{4a}$$

or alternatively, considering orthogonality of eigenvectors (i.e., $\sum_{l=0}^{L} \sum_{m=-l}^{l} g_{n',lm} g_{n,lm} = \delta_{nn'}$, where $\delta_{nn'} = 1$ if $n = n'$; otherwise $\delta_{nn'} = 0$), we obtain the following:

$$s_n = \sum_{l=0}^{L} \sum_{m=-l}^{l} s_{lm} g_{n,lm}. \tag{4b}$$

[9] In this study, we focused on the area significantly affected by the 2004 great Sumatra-Andaman earthquake extending from 10°S to 20°N latitudes and from 80°E to 110°E longitudes (Figure 1). The maximum degree of expansion we used to model the gravity signal from

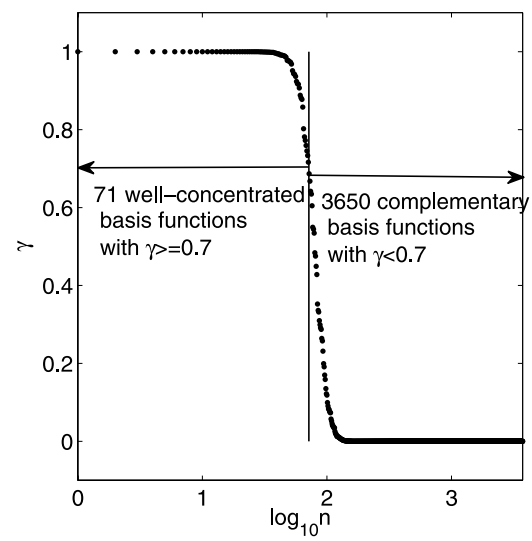

Figure 2. Concentration ratio γ for all band-limited Slepian functions. Value n (index of the Slepian basis function) = 1, 2, . . ., 3721 (= 61^2). There are 71 well-concentrated functions in the predefined domain (see Figure 1 and the text for the area used) and 3650 other functions that span the same vector space spanned by usual spherical harmonic basis functions with the maximum expansion degree of 60. Most of the functions with a concentration ratio smaller than 0.7 are well concentrated outside the study region referred to as the complementary region.

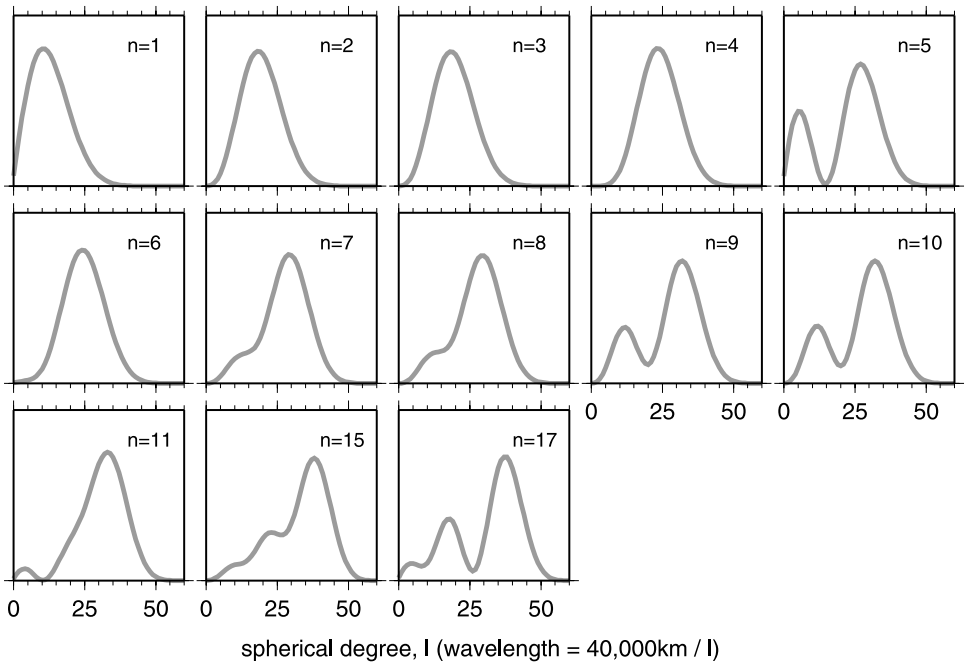

Figure 3. Degree power spectra of each (band-limited) basis function shown in Figure 1.

GRACE data is 60 which is the maximum degree of the level 2 (L2) products available from GRACE project website (http://podaac.jpl.nasa.gov/grace/). Therefore, there are 61^2 orthogonal basis functions spanning the vector space over the globe (for a band-limited harmonic function). After solving the eigenvalue problem (or maximization problem), we obtained the Slepian functions (eigenvector) and the corresponding concentration ratio (eigenvalue) of each Slepian basis.

[10] Figure 1 shows spatial patterns of some basis functions concentrated in our region. Figure 2 shows the concentration ratio for all Slepian basis functions. The number of the well-concentrated functions with the ratio greater than 0.7 is 71, and the rest of the 3650 (= 61^2-71) functions are less concentrated in our region of interest and many of them are well concentrated outside of our region. Both well-concentrated and complementary ones span the same vector space spanned by usual spherical harmonic basis functions. However, unlike spherical harmonic basis functions, the energy distribution of these new functions depends on geographical location.

[11] The basis functions shown in Figure 1 have the concentration ratio greater than 0.999999, indicating most of energy of the function is concentrated within the region (less than 0.0001% of energy leaks outside of the region). The degree power spectrum of each function, defined by $c_n(l) = \sum_{m=-l}^{l} |g_{n,lm}|^2$, where l is spherical harmonic degree and the corresponding wavelength is computed by 40,000 km/l, is depicted in Figure 3. They are orthogonal in the region and practically orthonormal differing from the exact normality within the region only by <0.0001% (and exactly orthonormal in the entire globe) as also indicated by equation (35) of *Simons and Dahlen* [2006]. However, the Slepian basis function yields a broad spectral range of the energy distribution as shown in Figure 3. Note that the Slepian function is nothing but lumped spherical harmonic functions. As n increases, the peak of the primary lobe for the energy distribution gradually moves toward higher degrees and the eigenvalue (concentration ratio) decreases. For example, the peak power of the first Slepian function locates at degree 10 while that of the fourth Slepian does at degree 23. The second and third functions present almost the same spectral power contents but differ only in azimuth or orientation. In section 4, we discuss the error estimates of those functions from GRACE data, and we show that they are quite different owing to GRACE's nonisotropic observing sensitivity.

[12] In section 3, we describe how we modeled the surface mass and the corresponding gravitational acceleration along the satellite orbit. We discuss how we estimated mean mass variation in the region every 15 days from the overflight satellite-tracking data by means of new regional basis functions and by applying the fundamental derivations developed by *Han et al.* [2008].

3. Observation Equation of Intersatellite Tracking Data

[13] The primary measurement used for detecting time-variable gravity is the change in the intersatellite range between the two identical satellites that are separated roughly by 220 km and are orbiting around the Earth at 450 km altitude. The rate of intersatellite range measurement can be expressed using the relative position vector $\mathbf{r}_{12}(t)$ and relative velocity vector $\mathbf{v}_{12}(t)$ as follows:

$$\dot{\rho}(t) = \mathbf{v}_{12}(t)^T \mathbf{r}_{12}(t) \Big/ \sqrt{\mathbf{r}_{12}(t)^T \mathbf{r}_{12}(t)}. \tag{5}$$

As shown by *Han et al.* [2008], the relative state vectors that appear in equation (5) are a linear combination of the a priori relative states $\tilde{\mathbf{r}}_{12}(t)$ and $\tilde{\mathbf{v}}_{12}(t)$, the initial relative

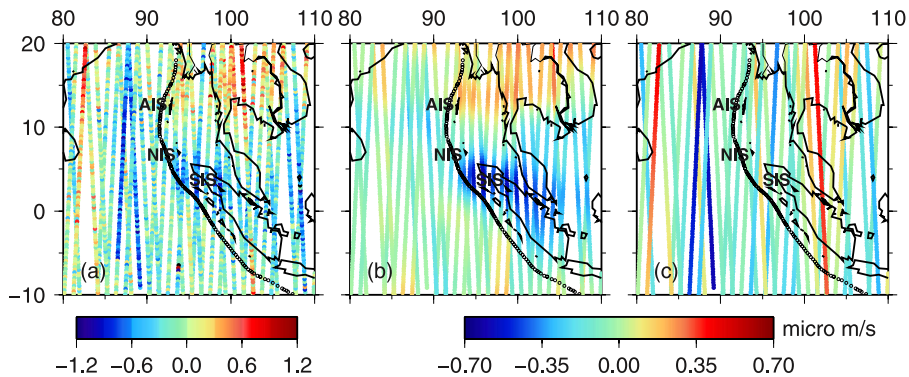

Figure 4. (a) Gravity Recovery and Climate Experiment (GRACE) range-rate residual observations and ground tracks for the first 15 days in July 2005 with the scale bar ranging ±1.2 μm/s. After the inversion, the range-rate perturbations are predicted from the regional mass variation and relative initial state. (b) Regional mass variation. (c) Relative initial state. Note that Figures 4b and 4c are depicted with a scale ranging ±0.7 μm/s. AIS, NIS, and SIS indicate Andaman, Nicobar, and Sumatra Islands, respectively. The location of Java (Sunda) trench is depicted by small black circles.

states $\delta\mathbf{r}_{12}^0$ and $\delta\mathbf{v}_{12}^0$, and the time integral of the relative acceleration vector $\delta\mathbf{a}_{12}$:

$$\mathbf{r}_{12}(t) = \tilde{\mathbf{r}}_{12}(t) + \delta\mathbf{r}_{12}^0 + \int_{t_0}^{t}\int_{t_0}^{t'} \delta\mathbf{a}_{12}(t'')dt''dt', \tag{6}$$

$$\mathbf{v}_{12}(t) = \tilde{\mathbf{v}}_{12}(t) + \delta\mathbf{v}_{12}^0 + \int_{t_0}^{t} \delta\mathbf{a}_{12}(t')dt'. \tag{7}$$

The a priori state vectors are calculated on the basis of the mean Earth gravity model such as GGM02C [*Tapley et al.*, 2004a] and other temporal gravitational models including planetary perturbation, body tides, ocean tide, atmosphere and ocean mass, and nongravitational force from onboard measurements, as described by *Luthcke et al.* [2006b]. Therefore, the deviation of the actual orbital state vector from the calculated state vector is caused primarily by unmodeled temporal change in the gravity field with respect to the applied mean field. *Han et al.* [2008] showed detailed derivations relating the measurements and the surface mass anomaly by expressing the relative acceleration vectors by means of mass anomaly uniformly distributed on the surface grid. In this study, we modified the observation equations by introducing the Slepian basis function for representing the relative acceleration vectors as follows:

$$\delta\mathbf{a}_{12}(t) = \mathbf{R}_b^i(t)\sum_{n=1}^{N} s_n \mathbf{a}_{12}^n(t), \tag{8}$$

where $\mathbf{R}_b^i$ is a rotation matrix to transform a vector in the body fixed frame to the inertial frame and s_n are the Slepian coefficients to be estimated. The time integration of the relative acceleration vector for equations (6) and (7) is performed numerically in the inertial frame. N is the total number of Slepian basis functions applied in the analysis, which is typically much less than the number of spherical harmonic coefficients. As indicated in section 2, in our case, $N = 71$ and is sufficient to represent most of the (band-limited) signal originating from our region. The relative acceleration vector contributed from the nth Slepian basis, $\mathbf{a}_{12}^n$, is computed by taking derivatives of the gravitational potential in radial, north (colatitude), and east (longitude) directions. After applying equation (4a), it is given explicitly by

$$\mathbf{a}_{12}^n(r_1,\theta_1,\lambda_1,r_2,\theta_2,\lambda_2) = \frac{GM}{R_E}\sum_{l=0}^{L}\sum_{m=-l}^{l} g_{n,lm}\left(\begin{bmatrix}\dfrac{\partial}{\partial r_1}\\ \dfrac{\partial}{r_1\partial\theta_1}\\ \dfrac{\partial}{r_1\sin\theta_1\partial\lambda_1}\end{bmatrix}\left(\frac{R_E}{r_1}\right)^{l+1} Y_{lm}(\theta_1,\lambda_1) - \begin{bmatrix}\dfrac{\partial}{\partial r_2}\\ \dfrac{\partial}{r_2\partial\theta_2}\\ \dfrac{\partial}{r_2\sin\theta_2\partial\lambda_2}\end{bmatrix}\left(\frac{R_E}{r_2}\right)^{l+1} Y_{lm}(\theta_2,\lambda_2)\right), \tag{9}$$

where (r_1, θ_1, λ_1) and (r_2, θ_2, λ_2) are spherical coordinates (radius, colatitude, longitude) of the two satellites, GM is the multiplication of gravitational constant and Earth mean mass, and R_E is the mean radius of the spherical Earth.

[14] The Slepian coefficients and the relative state vectors are linearly related via equations (6) and (7). However, the relationship between the observations (range rate) and relative state vectors are nonlinear, which yields a nonlinear relationship between the observations and the parameters to be solved, that is, Slepian coefficients. We take the partial derivatives of the observation equation with respect to the unknown parameters including the Slepian coefficient vector $\mathbf{s}$ ($N \times 1$ vector) and relative initial state vectors $\delta\mathbf{r}_{12}^0$ and

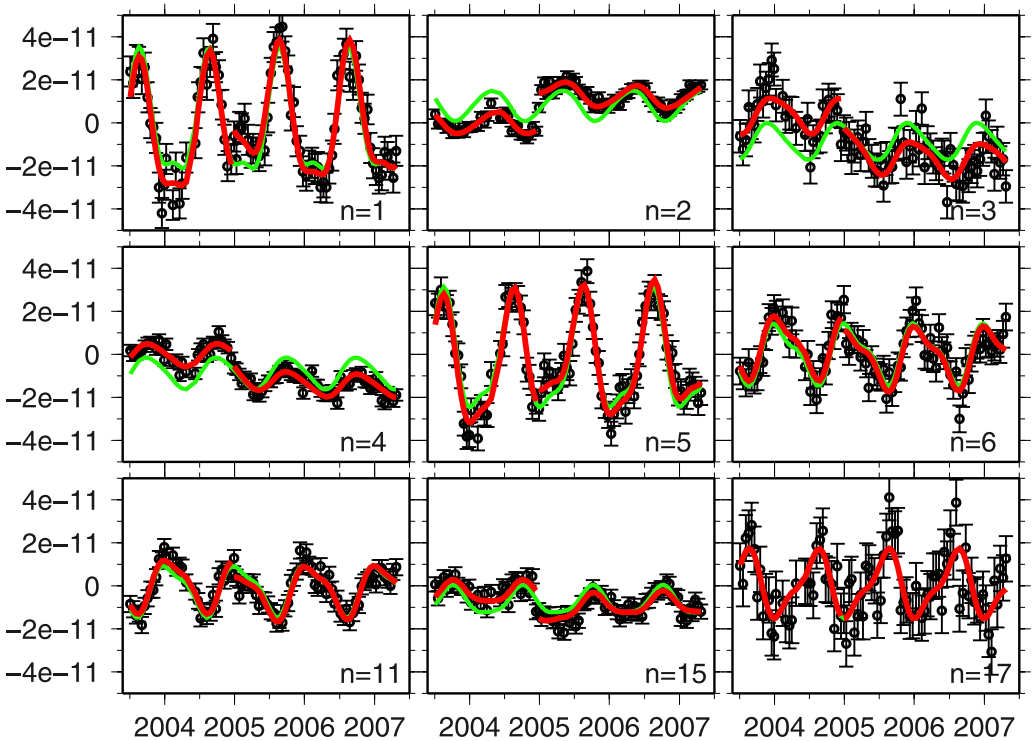

Figure 5. Time series of some Slepian coefficient estimates implying 15-day mean mass variation within the region. The least squares fits with a model with annual and semiannual sinusoids are shown in green (equation (12) in the text), and a model with two sinusoids as well as a step and an exponential function is shown by red lines (equation (13) in text). The time series of n = 17 indicates there is no significant step and/or exponential parameters after the statistical hypothesis test. Refer to equation (11) to see how these coefficients are related to the gravity on the surface.

$\delta\mathbf{v}_{12}^0$ for each arc. The linearized observation equation is given by

$$\delta\dot{\rho}(t) = \dot{\rho}(t) - \tilde{\dot{\rho}}(t) \approx \begin{bmatrix} \frac{\partial\dot{\rho}(t)}{\partial\mathbf{s}} & \frac{\partial\dot{\rho}(t)}{\partial\delta\mathbf{r}_{12}^0} & \frac{\partial\dot{\rho}(t)}{\partial\delta\mathbf{v}_{12}^0} \end{bmatrix} \begin{bmatrix} \mathbf{s} \\ \delta\mathbf{r}_{12}^0 \\ \delta\mathbf{v}_{12}^0 \end{bmatrix} + e, \tag{10}$$

where $\dot{\rho}$ is the observed range rate with the associated error e and $\tilde{\dot{\rho}}$ is the calculated range rate from the calculated relative state vectors $\tilde{\mathbf{r}}_{12}(t)$ and $\tilde{\mathbf{v}}_{12}(t)$.

[15] Figure 4a shows the actual range-rate residual data $\delta\dot{\rho}$ along the satellite ground tracks over the study area for the first 15 days of July in 2005. As described by *Han et al.* [2008], the initial relative state vectors $\delta\mathbf{r}_{12}^0$ and $\delta\mathbf{v}_{12}^0$ (arc-dependent parameter) were estimated in addition to the Slepian coefficients vector $\mathbf{s}$ (common parameter) accounting for the mean surface mass variation in the region. The least squares inversion was performed with the observation equation given in equation (10). With the estimated coefficient vector $\mathbf{s}$ and initial state vectors $\delta\mathbf{r}_{12}^0$ and $\delta\mathbf{v}_{12}^0$, their contributions to the range-rate perturbations were predicted separately and shown in Figures 4b and 4c, respectively. While the variations such as shown in Figure 4b, represented by the Slepian coefficients, are due to the mass variation in the region, the long-wavelength perturbations included in some short arcs of range-rate residual data are presumably caused by errors in accelerometer measurements and errors in the applied force models. The residuals, realized by removing Figures 4b and 4c from Figure 4a, look more or less random and yield 0.19 μm/s of root-mean-square (RMS), which is known to be the KBR instrument error level [*Luthcke et al.*, 2006b].

[16] Using the estimated Slepian coefficients, we can evaluate the gravity (radial derivative of potential) change, $\delta\zeta$, at mean sea level as follows:

$$\delta\zeta(\theta,\lambda) = \frac{GM}{R_E^2}\sum_{n=1}^{N} s_n \sum_{l=0}^{L}\sum_{m=-l}^{l} g_{n,lm}(l+1)Y_{lm}(\theta,\lambda). \tag{11}$$

The geoid change and other related quantities are easily computed only by changing the degree-dependent factor [*Heiskanen and Moritz*, 1967].

4. Time Series of the Slepian Coefficient Estimates

[17] The time series of 15-day mean Slepian coefficients associated with several representative basis functions are shown in Figure 5. Those corresponding to n = 1, 2, 3, 4, 5, 6, 11, 15, and 17 Slepian basis functions are presented. For every time series, we attempted to fit the temporal variation of the coefficients by analytical functions composed of annual and semiannual sinusoids, a step, and an exponential function to account for the effects of seasonal fluctuations

caused by climate-related signals (such as terrestrial hydrology and ocean mass), coseismic change, and postseismic change, respectively. We tested two analytic models for the least squares fits. The first model M1 includes only two sinusoids (annual and semiannual) and an offset as follows:

$$s_n(t_i) = A\cos(2\pi f_a t_i) + B\sin(2\pi f_a t_i) + C\cos(2\pi f_{sa} t_i) + D\sin(2\pi f_{sa} t_i) + E + e, \quad (12)$$

where f_a and f_{sa} are the annual and semiannual frequencies, respectively, and e is noise in the GRACE estimate of s_n. The coefficients A through E are associated with the seasonal climate signals. The second model M2 was modified from M1 by including the two additional parameters for the step where the jump is located at the epoch of the 2004 great Sumatra-Andaman earthquake and for the exponential function after the step, expressed as $1-\exp(-t/\tau)$ where t is time elapse since the earthquake and τ = 150 days. We did not attempt to estimate τ but fixed it as a constant. The explicit form for M2 is given as

$$s_n(t_i) = A\cos(2\pi f_a t_i) + B\sin(2\pi f_a t_i) + C\cos(2\pi f_{sa} t_i) + D\sin(2\pi f_{sa} t_i) + E + Fh(t_i, t_{eq}) + G\{1 - \exp(-(t_i - t_{eq})/\tau)\} + e, \quad (13)$$

where $h(t_i, t_{eq}) = 0$ for $t_i < t_{eq}$ and $h(t_i, t_{eq}) = 1$ for $t_i \geq t_{eq}$. t_{eq} is the earthquake epoch. The coefficients F and G indicate the amount of coseismic and postseismic changes, respectively.

[18] The green and red lines in Figure 5 represent the least squares fits with M1 and M2, respectively. The error bars in Figure 5 were calculated by means of postfit residuals (data after subtracting the least squares fit using the model including step and exponential parameters). For the n = 1 component of the Slepian function, spatially representing an overall mean in the region (see Figure 1), the seasonal variation dominates; however, the abnormal variation during the low-signal period from late 2004 to mid 2005 was better modeled when the step and exponential parameters were included. For the n = 2 function, showing the dipole anomaly along the north-south direction, the earthquake signal is dominant (with smaller seasonal variations). The quality of the fit is greatly enhanced by including the two additional earthquake parameters. For n = 3 representing the same dipole anomaly but along the east-west direction, the amount of coseismic jump is as large as the amplitude of seasonal change. Notably, the error associated with the n = 3 function is much greater than the error for n = 2 although the spectral power of both basis functions are almost identical (see Figure 3; they are different only in orientation). This highlights that GRACE measurements are particularly sensitive in the north-south direction and thus the accuracy depends on the orientation. This confirms the previous study results based on the correlation of GRACE monthly spherical harmonic coefficients and various geophysical models [*Han et al.*, 2005] and also discussed by *Swenson and Wahr* [2006]. For the rest of the cases in Figure 5, the earthquake parameters are a significant contribution to the observed time series, except for the case of n = 17. As we will see in section 5, the Slepian basis of n = 17 contains the coseismic signal predicted from the model to be as large as the case of n = 3 and larger than the case of n = 4. However, the GRACE observations are too noisy to detect it and just the seasonal change is discernible. As can be seen from Figure 1, this particular function looks very similar to the typical error pattern in GRACE observations, that is, "stripes" [e.g., *Swenson and Wahr*, 2006]. Also note that the overall spectral contents of function of n = 15 is similar with those of n = 17; however, the time series of n = 15 is much less scattered owing to the distinct spatial pattern that can be better resolved from GRACE observations.

[19] Figure 6 shows the same GRACE times series as shown in Figure 5 but after removing the seasonal (annual and semiannual) sinusoidal components. The abrupt change at the time of the earthquake and the following exponential decay were found in many of the time series.

[20] Here we estimate and discuss the abrupt change observed in the time series of the Slepian coefficients on the basis of the alternate earthquake slip models constrained by seismic and GPS data spanning different coseismic time intervals. The seismic slip model considered here is a modification of Model III of *Ammon et al.* [2005], which was also discussed earlier by *Han et al.* [2006]. In this study, we improved the fault geometry by considering the curvature of subduction interface along the downdip direction. The dip angles of shallower fault segments are about half of the corresponding fault segment of Model III. The models were computed using 111 seismic waveforms within periods ranging from 20 s to 2000 s and 34 "close-fault" (the shortest distances to the fault plane is less than 100 km) and 32 "distant" (300 km to 1100 km) GPS vectors from the published literature [*Gahalaut et al.*, 2006; *Subarya et al.*, 2006; *Vigny et al.*, 2005]. In order to address the abnormally large, immediate postseismic deformation (probably 25% to 35% of the main shock during the first day [*Banerjee et al.*, 2005]), we introduced a physically plausible combined inversion procedure. We simultaneously inverted the slip of two fault models (coseismic and the first-day postseismic models), which have identical geometry, but have different contributions to the observations. The first fault model (coseismic model) was used to simulate the coseismic rupture during the first 10 min. It radiates the seismic waves and also generates the static displacements. The second fault model (short-term afterslip model) aims to simulate the 1-day accumulated slow slip that affects the GPS observations without generating seismic waves. Following *Han et al.* [2006], the gravity change was computed considering vertical deformation of each layer with a distinct density and volume strain change (density variation) inside of the layered half-space Earth model. We decomposed the gravity change map computed from the coseismic (10 min) and 1-day afterslip models into the Slepian basis functions. We used equation (11) to compute s_n up to $N = 71$ from the grid gravity maps $\delta\zeta(\theta, \lambda)$.

[21] Depicted in Figure 6 are the model predictions from the 10-min coseismic slip (green lines) and with 1 day of afterslip added (blue lines) and from another independent 1-day "coseismic" slip model (magenta lines) constrained only by GPS data from *Banerjee et al.* [2007] and *Pollitz* [2006]. The least squares fit for earthquake parameters (one for amplitude of the step and the other for amplitude of the exponential change) to the GRACE data is drawn in red. The model agrees better with the GRACE observations

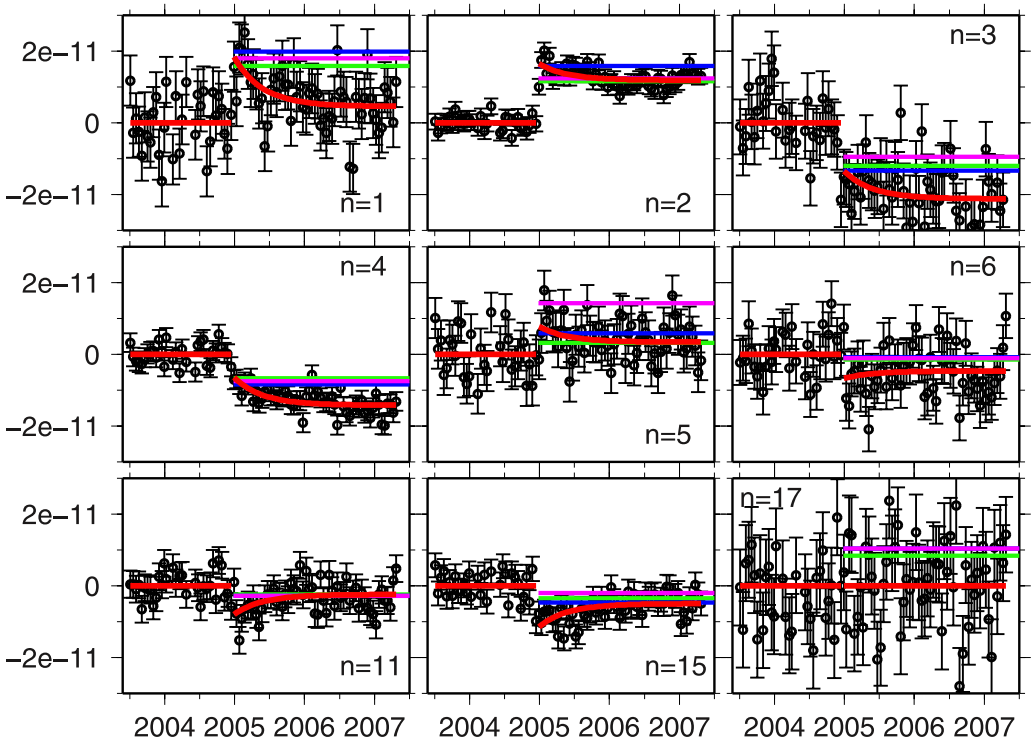

Figure 6. The same as Figure 5 but after subtracting the annual and semiannual sinusoids from the observations. Depicted also are the predicted coseismic changes (1-day accumulated slip) from the models constrained by seismic and GPS data (blue lines) and by GPS data only (magenta lines). The effect of the 10-min seismic slip is shown with green lines. The step and exponential fit (two parameters) to each of the time series is shown with red lines.

when the 1-day afterslip is added (blue lines) to the 10-min seismic slip (green lines). The two models (blue and magenta lines) are quite consistent except for the case of n = 5, where GRACE favors the one constrained by both seismic and GPS data. The models underestimate the coseismic change for the cases of n = 6, n = 11, and n = 15. For the case of n = 17, GRACE is too noisy (as also mentioned above) although the models indicate there is a significant change.

[22] From the time series of the first and second Slepian coefficients (n = 1 and n = 2), the coseismic (and 1-day afterslip) models explain remarkably well the significant jumps in the GRACE observations. The afterslip (from 10 min to 1 day) increases gravity change by ∼20%. The

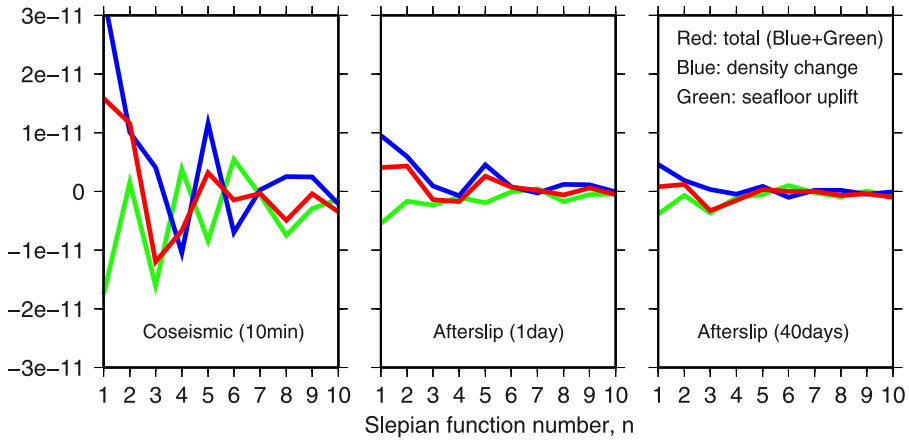

Figure 7. The model coefficients decomposed with Slepian basis function for n = 1, 2, . . ., 10: (left) 10-min seismic slip, (middle) 10-min to 1-day afterslip, and (right) 1-day to 40-day afterslip. The gravity effects from surface deformation (green lines) and from the density change and interface deformation (blue lines) are considered separately. The total gravity change (red lines) should be equal to the sum of both effects (green + blue).

postseismic gravity changes are observed to decrease exponentially over a timescale of several months (~150 days). The amount of decrease is greater in the first basis than the second one. The abrupt gravity change observations in the third and fourth basis functions agree well with the coseismic models, and the corresponding postseismic gravity changes increase with time, unlike the cases of n = 1 and 2.

[23] We also used the intermediate-term afterslip model from day 1 to day 40 [*Chlieh et al.*, 2007] that indicates downdip slow slip accumulation. Figure 7 shows the Slepian coefficients (for n = 1, 2, ..., 10) of the gravity changes from the coseismic, short-term afterslip, and intermediate-term afterslip. For the coseismic gravity change (Figure 7, left), the effect of density change (blue lines) in the total gravity change (red lines) is greater than the effect of the surface uplift (green lines) for the cases of n = 1 and n = 2. However, the effect of coseismic uplift is greater for the case of n = 3 which is consistent with the fact that the basis of n = 3 shows a typical pattern for seafloor uplift and subsidence for the faults with strike angles greater than 300° and with the dominant dip-slip mechanism. The afterslip from 10 min to 40 days causes additional changes amounting to 25%–30% of the coseismic gravity change (~10 min). The afterslip tends to amplify the coseismic gravity change in most cases. The gravity change from afterslip (accumulated from day 1 to day 40) is dominant at the basis of n = 3. The postseismic variation differs in magnitude from the coseismic changes depending on the spatial frequency and orientation of the anomaly. The exponential changes with a timescale of some months prevail in several Slepian coefficients estimated by regional GRACE analysis. The afterslip model alone could not explain the dominant relaxation pattern in GRACE observations, especially for n = 1 and n = 2.

5. Inference to Postseismic Mechanism and Earth's Viscosity Structure

[24] In section 4, it was observed that GRACE time series contain a significant abrupt change with a magnitude that partially depends on the coseismic time interval and exponential decay with the empirically determined time factor (τ) of 150 days. The observation of coseismic (episodic) gravity change could not be explained without including the intrinsic density change for the (long-wavelength) gravity modeling [*Han et al.*, 2006]. In this section, we analyze the exponential decay pattern with more than 2 years of data after the earthquake. After we tested various Earth viscosity models against the GRACE observations, we quantified the most plausible viscoelastic signatures of the Earth from the observations.

[25] For the viscoelastic modeling, we used the viscoelastic structure of the Earth given in Figure 2 of *Pollitz et al.* [2006], with variations as noted below. For example, the vertical density structure is from Preliminary Reference Earth Model (PREM) [*Dziewonski and Anderson*, 1981]. The upper (220–670 km) and lower (670–2891 km) mantle were modeled with a Maxwell rheology with the viscosity of 10^{20} Pa s and 10^{21} Pa s, respectively. For the asthenosphere between 62 km and 220 km depth, the rheology was modeled for the following five cases: (1) Maxwell viscosity of 5×10^{17} Pa s, (2) 10^{18} Pa s, (3) 5×10^{18} Pa s, (4) 10^{19} Pa s, and finally (5) transient (Kelvin) viscosity of 5×10^{17} Pa s and steady state (Maxwell) viscosity of 10^{19} Pa s with biviscous (Burgers body) rheology [*Ivins*, 1996]. All parameters were fixed except the asthenosphere viscosity. The lithosphere layer (0–62 km) was assumed to be purely elastic and assigned a very large viscosity value such as 10^{30} Pa s.

[26] We used the computer code VISCO1D [*Pollitz*, 1997a] to compute the postseismic response to dislocation sources for alternate spherical viscoelastic models. Modeled postseismic gravity changes were derived in two ways: (1) by computing the gravity effect of postseismic vertical displacement of the interface between two layers with distinct densities and numerically integrating postseismic density change over a large volume of the deforming Earth around the study area and (2) by using analytic formulae for the viscoelastic gravity response as a function of spherical harmonic degree following *Pollitz* [1997b]. The two approaches are redundant and serve as a check on one another; that is, they yielded almost identical results within only a few percent.

[27] The snapshot of cumulative postseismic gravity changes were computed at 0.1, 0.2, 0.3, 0.5, 1, 2, 3, 5, and 10 years after the earthquake. The individual gravity map data were decomposed using the Slepian basis functions, and the time series of each model coefficient were obtained by a linear interpolation from the data point at aforementioned epochs for all five hypothetical cases. Figure 8 shows the time series of the Slepian coefficients n = 1, 2, 3, and 4 from GRACE observations (black and thick gray for the least squares fit) and from the models with various hypothetical asthenosphere viscosity models (colored lines).

[28] For n = 1, the observed coseismic gravity change decreases postseismically by ~60% within 6 months (from $\sim 2 \times 10^{-11}$ to $\sim 0.8 \times 10^{-11}$). The low Maxwellian viscosity (5×10^{17}–10^{18} Pa s) reasonably explains the observations within 6 months after the earthquake. However, it fails to explain the observations thereafter. The observations after year 2006 follows the trend (mostly linear) predicted from the Maxwell model with viscosities of 5×10^{18}–10^{19} Pa s. None of the Maxwell viscosity models suitably explains more than 2 years of the GRACE observations after the earthquake. The agreement greatly improves when we consider a biviscous model with the transient viscosity of 5×10^{17} Pa s and the steady state viscosity of 10^{19} Pa s. The gravity variation with the (steady state) viscosity variation is not linear. For example, the gravity variation is more drastic when the Maxwell viscosity varies from 10^{18} Pa s to 5×10^{18} Pa s (cyan to blue) than when it varies from 5×10^{18} Pa s to 10^{19} Pa s (blue to magenta). It implies these short-term, large-scale satellite gravity measurements are most sensitive to viscosity when it is smaller ($<\sim 5 \times 10^{18}$ Pa s). The observations favor the steady state viscosity within the range of 5×10^{18}–10^{19} Pa s. The two or so years of GRACE data with an error bar of 0.7×10^{-11} do not fully discriminate the steady state viscosity within such range. However, with the future inclusion of more data extended to the end of the GRACE mission (year 2010 or so), the gravity observations should be able to narrow the range of the steady state viscosity estimates that account for the postseismic decay.

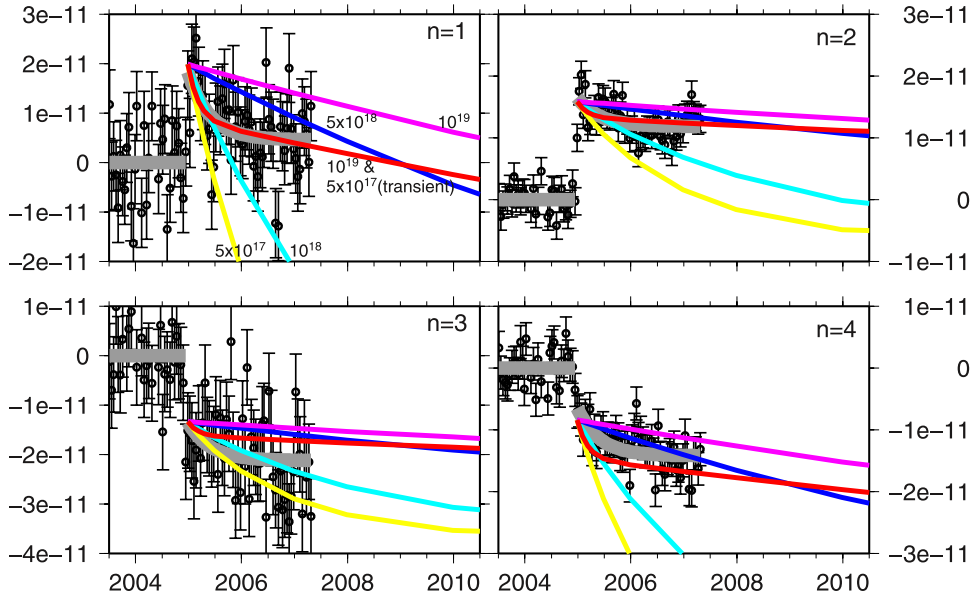

Figure 8. The time series of the first four Slepian coefficients estimates (black lines) and its least squares fit (thick gray lines). Depicted are the predicted postseismic viscoelastic gravity changes from various Earth viscosity models. The gravity changes from the assumed Maxwell asthenosphere with the viscosity of 5×10^{17} Pa s (yellow lines), 10^{18} Pa s (cyan lines), 5×10^{18} Pa s (blue lines), and 10^{19} Pa s (magenta lines) and the gravity change from the biviscous (Burgers body) asthenosphere with the transient viscosity of 5×10^{17} Pa s and steady state viscosity of 10^{19} Pa s (red lines) were computed. The upper and lower mantle viscosities (Maxwell rheology) were assumed to be 10^{20} and 10^{21} Pa s, respectively, for all cases.

[29] For n = 2, the transient behavior is relatively small but still clearly distinguishes between unfavorable models with the smaller Maxwell viscosities. However, the coefficients of n = 2 may not be useful in refining the range of steady state viscosity estimates even with the GRACE observations to 2010. For n = 3, it is not clear whether the observations are better explained with Maxwell rheology or biviscous rheology with two years of data. The difficulty is due to large errors associated with the less observational sensitivity of GRACE measurements to the pattern such as n = 3. The larger magnitude of the exponential change in the GRACE observations than the biviscous model prediction may be explained by an additional contribution from afterslip downdip of the rupture zone. Note that the afterslip to 40 days is greatest at n = 3 as shown in Figure 7. The GRACE observations for the Slepian coefficient of n = 4 show that the transient postseismic variation of about 1-year duration is as large as the coseismic variation. It clearly supports the biviscous model. Again, the estimated steady state viscosity range of 5×10^{18}–10^{19} Pa s can be further improved with a longer time series of observations.

[30] If the time series of each coefficient are interpreted along with the corresponding spatial pattern given in Figure 1, one sees an abrupt large negative gravity change around the northern tip of Sumatra Island and subsequent decrease from n = 1. The instantaneous negative gravity change is due primarily to the density change (dilatation in crust), associated with the coseismic rupture and immediate afterslip. However, the gradual relaxation of the gravity thereafter is due mostly to postseismic seafloor uplift. According to our model computation, the postseismic gravity change caused by the density change and vertical displacement at internal density discontinuities is as small as 10% of the effect associated with the seafloor uplift. For coseismic slip, the elastic deformation occurs instantaneously and therefore it is expected to yield density changes in all layers. For postseismic relaxation, the changes occur more slowly and the gradual density changes would be small, but the surface uplift or subsidence would be cumulative and dominant.

[31] From the pattern of n = 2 (Figure 1), we can recognize that a coseismic gravity increase occurred south of the trench, and a simultaneous decrease occurred in Andaman Sea, with both being followed by postseismic relaxation. The abrupt change is due partly to density change and/or subsidence (negative in Andaman Sea) and partly to seafloor uplift (positive in south of the trench). The pattern of n = 3 indicates abrupt positive gravity change and exponential increase west of the trench, and negative gravity change in Andaman Sea. It is likely due to the coseismic seafloor vertical deformation and its postseismic continuation, considering the fault plane with the strike of ~340° and the prominent dip slip faulting mechanism. In this case, the afterslip (40 days) plays a greater role than does the viscoelastic deformation (Figure 7). It is difficult to provide physical interpretations for other, more complicated, spatial patterns of the Slepian functions (mathematically derived without consideration for earthquake physics or mechanism).

[32] The postseimsic gravity signal-to-noise ratio (SNR) is computed for each of the Slepian coefficients by using the postfit residuals for error realization. The predicted signal is

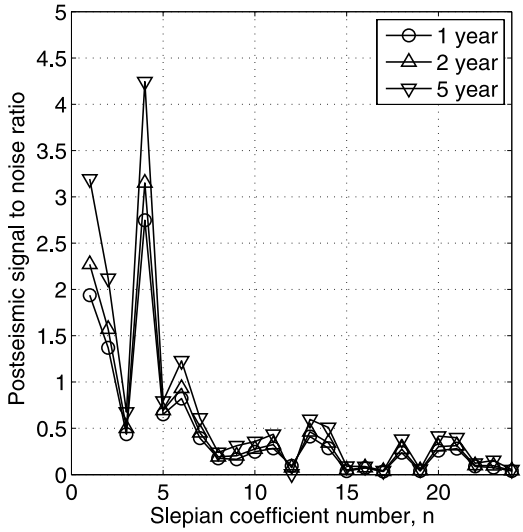

Figure 9. The postseimic gravity signal-to-noise ratio at 1, 2, and 5 years after the earthquake. The biviscous model predictions are used for representing the signal.

represented by the biviscous model. Figure 9 shows the SNR over n (s_n/e_n) for 1, 2, and 5 years after the earthquake. It indicates that the most direct information for the postseismic gravity change is from n = 1, 2, and 4. We computed the spatial pattern of the postseismic gravity from these selected Slepian coefficients. We have chosen the first four coefficients because they are most significant (although SNR for n = 3 is less satisfactory). The exponential fit to the GRACE observation (thick gray in Figure 8) from the four Slepian coefficient estimates were used to compute the spatial pattern of the cumulative gravity change using equation (11). The accumulated postseismic gravity change using the biviscous model (red lines in Figure 8) was evaluated at year 2007. Figure 10a shows the biviscous model predictions without any filtering, and Figure 10b shows the model predictions using only the first four Slepian coefficients for consistent comparison with GRACE "filtered" observation that is shown in Figure 10c. The positive gravity change dominates around the Nicobar Islands, and the smaller ($\sim$−5 μGal) negative anomaly leads to good agreement between observations and model. Disagreement between the model (after filtering) and the observations appears mostly in the lack of positive anomaly in the observations around the northern Sumatra Islands. This is likely due to the poorly resolved Slepian coefficient for n = 3 where the observation coefficient is more negative than the model coefficient. The deviation of the observations (Figure 10c) from the "full-resolution" model (Figure 10a) is mostly due to poorly resolved variations in the east-west direction, which are particularly difficult to constrain using GRACE along-track measurements.

[33] The positive peak anomaly seen in Figure 10 is shifted inland (i.e., eastward) compared to the coseismic gravity change [*Han et al.*, 2006; *Pollitz*, 2006]. Unlike the coseismic gravity change, most of the postseismic gravity signal is explained by seafloor (and land) uplift with much smaller postseismic density change, indicating that the gradual deformation of the free surface (mostly uplift) has occurred postseismically without much internal strain change.

[34] The poroelastic response of the crust and upper mantle due to an earthquake could be an important postseismic deformation mechanism. The surface deformation associated with this mechanism has been numerically simulated for the 2004 Sumatra earthquake by *Masterlark* [2005] and *Masterlark and Hughes* [2007]. *Masterlark et al.* [2001] and *Freed* [2007] earlier reported localized deformation caused by poroelastic response that was suggested to occur mostly in the uppermost crust. Gravity change occurs by pore fluid (mass) redistribution as well as the associated deformation. Quantifying and numerically modeling the role of fluids in affecting the response of the upper mantle to an earthquake, as suggested by *Ogawa and Heki* [2007], may be important for determining if this effect could be detected with GPS and GRACE gravity.

6. Conclusions

[35] We analyzed the postseismic deformation following the 2004 Sumatra-Andaman earthquake in the time series of satellite gravity observations considering two mechanisms, postseismic slip (afterslip) and viscoelastic deformation. In

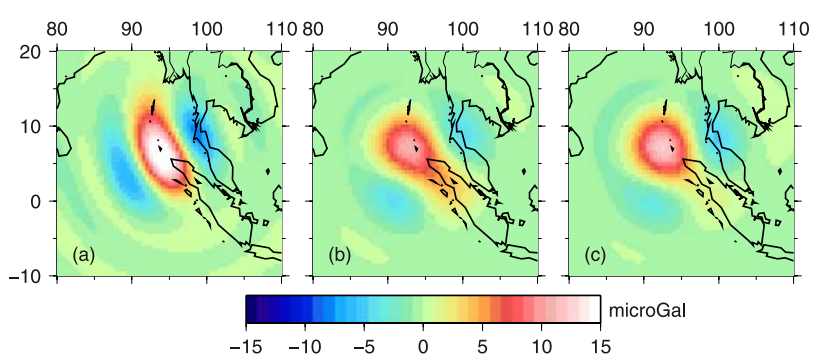

Figure 10. The spatial patterns of the postseismic gravity change from the biviscous model (2-year accumulation) and the GRACE observations (from the least squares estimates of the exponential function). (a) Model prediction without any filtering (using all coefficients). (b, c) Model prediction and GRACE observation, respectively, only using the first four Slepian coefficients yielding high SNR in the observations.

order to optimally process GRACE measurements with regard to the regionally intense gravity signature triggered by the 2004 great Sumatra-Andaman earthquake, we analyzed the satellite tracking data by means of regional basis functions. The Slepian basis functions are particularly suitable for analyzing the regional mass variations associated with large earthquakes since they are concentrated in the region, mutually orthogonal, and harmonic.

[36] The abrupt changes in the 15-day mean mass variations observed from GRACE data agree with the predictions of seismological and geodetic coseismic models in many of the Slepian coefficients, when we modeled the gravity change from the coseismic slip models considering density change as well as vertical displacement. Two years of postseismic GRACE gravity observations, which are well characterized by an exponentially decaying time function, were compared with various afterslip and viscoelastic models. The dominant relaxation pattern associated with the first two basis functions is opposite to what would be predicted from models of afterslip. However, the effects of afterslip seem to be largest in the third basis function showing the gravity variation along the east-west direction. In general, the GRACE observations are best accounted for by a biviscous asthenosphere model with the transient viscosity of 5×10^{17} Pa s and steady state viscosity of 5×10^{18}–10^{19} Pa s, which is consistent with the range of steady state viscosities found in many of subduction zone earthquake models [*Wang*, 2007]. More extended observations out to the end of the GRACE mission (year 2010 or so) could further improve the steady state viscosity estimates assuming no major interseasonal climate variation in the region.

[37] The afterslip mechanism explains the postseismic surface deformation observed at a limited number of near-field GPS sites (point-wise observations) for the 2004 Sumatra-Andaman earthquake [*Chlieh et al.*, 2007] and for the 2005 Nias-Simeulue earthquake [*Hsu et al.*, 2006]. The large-scale observation of postseismic gravity change, however, is most consistent with a (biviscous) viscoelastic relaxation model rather than postseismic slip downdip of the rupture zone. It should be emphasized that the spatial scale is important to the analysis of postseismic deformation mechanisms. We conjecture that the Earth viscosity structure is the most important factor to govern evolution of the long-wavelength stress field after the earthquake. Large-scale monitoring of the postseismic deformation from space will help characterize the rheological properties of the Earth's interior that may lead to a better understanding of continuing seismic hazard following great earthquakes.

[38] **Acknowledgments.** This work was supported by the U. S. National Aeronautical and Space Administration GRACE project and Earth Surface and Interior program. We acknowledge the NASA/GFZ GRACE project for the GRACE data products (distributed by JPL PODAAC) and colleagues at JPL for producing the quality Level 1B products. This work also benefited from the Goddard Space Flight Center's GEODYN software for computing the precise orbits. We thank Mohamed Chlieh for his afterslip model and Frederik Simons for clarification on the use of the spherical Slepian function. VISCO1D software and its upgrade with computation of the gravity component were used for the viscoelastic calculations. Some FORTRAN codes written by Mark Wieczorek were used (available at www.ipgp.jussieu.fr/~wieczor/SHTOOLS). We thank Roland Bürgmann, Kelin Wang, and an anonymous reviewer for constructive comments.

References

Ammon, C., et al. (2005), Rupture process of the 2004 Sumatra-Andaman earthquake, *Science*, *308*, 1133–1139, doi:10.1126/science.1112260.

Banerjee, P., et al. (2005), The size and duration of the Sumatra-Andaman earthquake from far-field static offsets, *Science*, *308*, 1769–1772, doi:10.1126/science.1113746.

Banerjee, P., F. Pollitz, B. Nagarajan, and R. Burgmann (2007), Coseismic slip distributions of the 26 December 2004 Sumatra-Andaman and 28 March 2005 Nias earthquakes from GPS static offsets, *Bull. Seismol. Soc. Am.*, *97*, S86–S102, doi:10.1785/0120050609.

Chen, J. L., C. R. Wilson, B. D. Tapley, and S. Grand (2007), GRACE detects coseismic and postseismic deformation from the Sumatra-Andaman earthquake, *Geophys. Res. Lett.*, *34*, L13302, doi:10.1029/2007GL030356.

Chlieh, M., et al. (2007), Coseismic slip and afterslip of the great Mw 9.15 Sumatra-Andaman earthquake of 2004, *Bull. Seismol. Soc. Am.*, *97*, S152–S173, doi:10.1785/0120050631.

Dziewonski, A. M., and D. L. Anderson (1981), Preliminary Reference Earth Model, *Phys. Earth Planet. Inter.*, *25*, 297–356, doi:10.1016/0031-9201(81)90046-7.

Freed, A. M. (2007), Afterslip (and only afterslip) following the 2004 Parkfield, California, earthquake, *Geophys. Res. Lett.*, *34*, L06312, doi:10.1029/2006GL029155.

Gahalaut, V. K., et al. (2006), Constraints on 2004 Sumatra-Andaman earthquake rupture from GPS measurements in Andaman-Nicobar Islands, *Earth Planet. Sci. Lett.*, *242*, 365–374, doi:10.1016/j.epsl.2005.11.051.

Han, S.-C., and F. J. Simons (2008), Spatiospectral localization of global geopotential fields from the Gravity Recovery and Climate Experiment (GRACE) reveals the coseismic gravity change owing to the 2004 Sumatra-Andaman earthquake, *J. Geophys. Res.*, *113*, B01405, doi:10.1029/2007JB004927.

Han, S.-C., et al. (2005), Non-isotropic filtering of GRACE temporal gravity for geophysical signal enhancement, *Geophys. J. Int.*, *163*, 18–25, doi:10.1111/j.1365-246X.2005.02756.x.

Han, S.-C., C. Shum, M. Bevis, C. Ji, and C. Kuo (2006), Crustal dilatation observed by GRACE after the 2004 Sumatra-Andaman earthquake, *Science*, *313*, 658–662, doi:10.1126/science.1128661.

Han, S.-C., D. D. Rowlands, S. Luthcke, and F. G. Lemoine (2008), Localized analysis of satellite tracking data for studying time-variable Earth's gravity fields, *J. Geophys. Res.*, *113*, B06401, doi:10.1029/2007JB005218.

Heiskanen, W., and H. Moritz (1967), *Physical Geodesy*, W. H. Freeman, San Francisco, Calif.

Hsu, Y. J., et al. (2006), Frictional afterslip following the 2005 Nias-Simeulue earthquake, Sumatra, *Science*, *312*, 1921–1926, doi:10.1126/science.1126960.

Ivins, E. R. (1996), Transient creep of a composite lower crust: 2. A polymineralic basis for rapidly evolving postseismic deformation modes, *J. Geophys. Res.*, *101*, 28,005–28,028.

Luthcke, S. B., H. J. Zwally, W. Abdalati, D. D. Rowlands, R. D. Ray, R. S. Nerem, F. G. Lemoine, J. J. McCarthy, and D. S. Chinn (2006a), Recent Greenland ice mass loss by drainage system from satellite gravity observations, *Science*, *314*, 1286–1289, doi:10.1126/science.1130776.

Luthcke, S. B., D. D. Rowlands, F. G. Lemoine, S. M. Klosko, D. Chinn, and J. J. McCarthy (2006b), Monthly spherical harmonic gravity field solutions determined from GRACE inter-satellite range-rate data alone, *Geophys. Res. Lett.*, *33*, L02402, doi:10.1029/2005GL024846.

Masterlark, T. (2005), Poroelastic coupling of the recent M9 and M8.7 earthquakes in the Sumatra-Andaman subduction zone, *Eos Trans. AGU*, *86*(52), Fall Meet. Suppl., Abstract U11A-0802.

Masterlark, T., and K. L. Hughes (2007), Evolution of deformation, pore pressure, and Coulomb stress following the M9 Sumatra-Andaman earthquake, *Eos Trans. AGU*, *88*(52), Fall Meet. Suppl., Abstract G21D-03.

Masterlark, T., C. DeMets, H. F. Wang, J. Stock, and O. Sanchez (2001), Homogeneous vs heterogeneous subduction zone models: Coseismic and postseismic deformation, *Geophys. Res. Lett.*, *28*, 4047–4050.

Ogawa, R., and K. Heki (2007), Slow postseismic recovery of geoid depression formed by the 2004 Sumatra-Andaman Earthquake by mantle water diffusion, *Geophys. Res. Lett.*, *34*, L06313, doi:10.1029/2007GL029340.

Panet, I., et al. (2007), Coseismic and post-seismic signatures of the Sumatra 2004 December and 2005 March earthquakes in GRACE satellite gravity, *Geophys. J. Int.*, *171*(1), 177–190, doi:10.1111/j.1365-246X.2007.03525.x.

Pollitz, F. F. (1997a), Gravitational-viscoelastic postseismic relaxation on a layered spherical Earth, *J. Geophys. Res.*, *102*, 17,921–17,941.

Pollitz, F. F. (1997b), Gravity anomaly from faulting on a layered spherical earth with application to central Japan, *Phys. Earth Planet. Inter.*, *99*, 259–271, doi:10.1016/S0031-9201(96)03204-9.

Pollitz, F. F. (2006), A new class of earthquake observations, *Science*, *313*, 619–620, doi:10.1126/science.1131208.

Pollitz, F. F., R. Burgmann, and P. Banerjee (2006), Post-seismic relaxation following the great 2004 Sumatra-Andaman earthquake on a compressible self-gravitating Earth, *Geophys. J. Int.*, *167*, 397–420, doi:10.1111/j.1365-246X.2006.03018.x.

Simons, F. J., and F. A. Dahlen (2006), Spherical Slepian functions and the polar gap in geodesy, *Geophys. J. Int.*, *166*, 1039–1061, doi:10.1111/j.1365-246X.2006.03065.x.

Simons, M., S. Solomon, and B. Hager (1997), Localization of gravity and topography: Constraints on the tectonics and mantle dynamics of Venus, *Geophys. J. Int.*, *131*, 24–44, doi:10.1111/j.1365-246X.1997.tb00593.x.

Slepian, D. (1983), Some comments on Fourier-analysis, uncertainty and modeling, *SIAM Rev.*, *25*, 379–393, doi:10.1137/1025078.

Subarya, C., et al. (2006), Plate-boundary deformation of the great Aceh-Andaman earthquake, *Nature*, *440*, 46–51, doi:10.1038/nature04522.

Swenson, S., and J. Wahr (2006), Post-processing removal of correlated errors in GRACE data, *Geophys. Res. Lett.*, *33*, L08402, doi:10.1029/2005GL025285.

Tamisiea, M. E., J. X. Mitrovica, and J. L. Davis (2007), GRACE gravity data constrain ancient ice geometries and continental dynamics over Laurentia, *Science*, *316*, 881–883, doi:10.1126/science.1137157.

Tapley, B. D., S. Bettadpur, M. Watkins, and C. Reigber (2004a), The gravity recovery and climate experiment: Mission overview and early results, *Geophys. Res. Lett.*, *31*, L09607, doi:10.1029/2004GL019920.

Tapley, B. D., S. Bettadpur, J. Ries, P. Thompson, and M. Watkins (2004b), GRACE measurements of mass variability in the Earth system, *Science*, *305*, 503–505, doi:10.1126/science.1099192.

Vigny, C., et al. (2005), Insight into the 2004 Sumatra-Andaman earthquake from GPS measurements in southeast Asia, *Nature*, *436*, 201–206, doi:10.1038/nature03937.

Wang, K. (2007), Elastic and viscoelastic models of subduction earthquake cycles, in *The Seismogenic Zone of Subduction Thrust Faults*, edited by T. H. Dixon and J. C. Moore, pp. 540–575, Columbia Univ. Press, New York.

S.-C. Han, S. B. Luthcke, and J. Sauber, Planetary Geodynamics Laboratory, Code 698, NASA Goddard Space Flight Center, Greenbelt, MD 20771, USA. (Shin-Chan.Han@nasa.gov)

C. Ji, Department of Earth Sciences, University of California, Santa Barbara, CA 93106, USA.

F. F. Pollitz, U.S. Geological Survey, Menlo Park, CA 94025, USA.